Xudong Zheng[1]
Assistant Professor
Department of Mechanical Engineering,
University of Maine,
Boardman Hall 213 A,
Orono, ME 04473
e-mail: xudong.zheng@maine.edu

Qian Xue
Department of Mechanical Engineering,
University of Maine,
Orono, ME 04473

Rajat Mittal
Department of Mechanical Engineering,
Johns Hopkins University,
Baltimore, MD 21218

Computational Study of Hemodynamic Effects of Abnormal *E/A* Ratio on Left Ventricular Filling

Three-dimensional numerical simulations are employed to investigate the hemodynamic effects of abnormal E/A ratios on left ventricular filling. The simulations are performed in a simplified geometric model of the left ventricle (LV) in conjunction with a specified endocardial motion. The model has been carefully designed to match the important geometric and flow parameters under the physiological conditions. A wide range of E/A ratios from 0 to infinity is employed with the aim to cover all the possible stages of left ventricle diastolic dysfunction (DD). The effects of abnormal E/A ratios on vortex dynamics, flow propagation velocity, energy consumption as well as flow transport and mixing are extensively discussed. Our results are able to confirm some common findings reported by the previous studies, and also uncover some interesting new features. [DOI: 10.1115/1.4027268]

Keywords: diastolic heart dysfunction, hemodynamics, left ventricular filling, biomechanics

1 Introduction

During one cardiac cycle, the freshly oxygenated blood in the left atrium (LA) enters the LV during two phases: the early (*E*) diastolic filling after the mitral valve opening in response to LV relaxation [1,2] and the late (*A*) diastole filling caused by atrial contraction [3]. The *E/A* ratio, which is defined as the ratio of the peak early (*E*) ventricular filling velocity to the peak late (*A*) ventricular filling velocity, is an important physiological index used in clinic practice to access the filling function of the LV [4,5]. In a healthy heart, most of the blood enters the LV during the early filling phase and the *E/A* ratio is usually between 1 and 2 [4]. This normal function is altered in patients with DD. In DD, the relaxation and compliance of the LV are impaired due to the stiffening of the ventricular wall [4], so the LV pressure during early diastole does not drop as much as in the normal heart and the early (*E*) filling velocity subsequently decreases. To preserve the ejection fraction (EF), the LA then needs to contract harder to squeeze out more blood during the late filling phase. This leads to an elevation of the ventricular pressure and hypertension [6]. At this stage of DD, the late filling velocity usually becomes higher than the early filling velocity, manifested by a reversed *E/A* ratio which is commonly accepted as an indication of impaired relaxation associated with early-stage DD [7]. With the prognosis of DD, the LA pressure progressively elevates and it subsequently restores the pressure drop between the LA and LV despite a slower rate of LV relaxation and an elevated LV pressure [7]. Under this condition, the early filling velocity returns to its normal level. Therefore, this stage of dysfunction is usually called the "pseudonormalization." At the final stage of dysfunction, the early filling velocity may become higher than the normal level, and dysfunction starts to affect the systolic function as well and finally leads to heart failure [4].

There is an increasing consensus that dynamics of the transmitral blood flow during the diastole plays a critical role in dictating the overall cardiac health and predicting early changes in cardiac functions [8–13]. For instance, the early diastolic filling has been shown dominated by the evolution of a vortex ring as the blood flows across the mitral valve from the LA into LV [14–17]. Gharib et al. [18,19] first discovered a universal dimensionless vortex formation time associated with the pinch-off of the leading vortex ring from the trailing jet in a piston-cylinder system and further found that there exists an optimal range of the vortex formation time for the LV vortex ring pinch-off in the normal healthy heart. Through a comparative study between the normal and pathological groups, they further proposed that this global index of vortex formation time is capable of identifying dysfunction related diseases at early stages [19] Kheradvar et al., [20]. The formation and evolution of the filing vortex ring inside the LV are asymmetric owing to the eccentric arrangement of the mitral orifice [9,11,21]. As the vortex ring convects downward, it is quickly dissipated on the posterior side closer to the myocardium wall, while the opposite anterior portion eventually evolves to a large rotational flow at the end of the diastole occupying the center of the ventricular cavity [16]. It is generally believed that this circulating flow pattern facilitates the redirection of the diastolic flow from the left atrium toward the aortic orifice, contributing to efficient pumping [21,22]. An alteration in the LV geometry and diastolic function could significantly modify the intraventricular flow pattern and energetic efficiency [23,24]. LV filling dynamics also affects other important aspects of ventricular functions, such as the filling velocity and pressure, filling energetic, blood transport and mixing, mitral annulus dynamics, ventricular wall relaxation, etc. [24,25–27]. Recently, several studies [16,17,19,28] have also established the quantitative links between the characteristics of intraventricular flow patterns and various heart dysfunctions with the aim to develop the strategies for reliable diagnosis of cardiac diseases.

Recognition of the close connection between intraventricular fluid dynamics and LV function motivated us to investigate the hemodynamic effects of DD on LV filling. In the current study, DD is characterized by an abnormal *E/A* ratio, which is also used as one of the indexes in the clinical setting to assess the severity of DD. Although flow structures in the LV have been extensively investigated by the imaging, experimental, and numerical studies, there is still only limited understanding of the changes in the intraventricular flow in various pathological conditions. Moreover, most of the past cardiac flow studies have been focused only on the intraventricular flow during the ventricular relaxation [9,14,29]. The effects of the more complex, multiphases filling

[1]Corresponding author.

Manuscript received July 2, 2013; final manuscript received March 14, 2014; accepted manuscript posted March 24, 2014; published online April 25, 2014. Assoc. Editor: Dalin Tang.

process on intraventricular fluid dynamics remain unclear. To this end, we aim to utilize the computational modeling to examine ventricular hemodynamics in the normal LV as well as the one with diastolic dysfunction during the entire diastole composed of three distinct phases: the ventricular relaxation (early filling), diastasis, and LA contraction (late filling). An immersed-boundary method (IBM) based incompressible Navier–Stokes flow solver is used to simulate the blood flows in a simplified geometric model of the heart in conjunction with a specified endocardial motion. This approach of combining the simplified heart model with a specified endocardial motion has been employed by many past studies. By carefully choosing all of the major geometric parameters and filling parameters, these simplified models can produce a reasonable representation of real cardiac flows [9,10,14,30–34]. This idealized approach also permits independent changes of parameters, such as *E/A* ratio and allows simulating the progression of diseases and separating out different biomechanical mechanisms associated with multiple pathological changes. The objective of the current study is to provide a better understanding of the fundamental flow features associated with left ventricular diastolic dysfunction (LVDD) characterized by abnormal *E/A* ratios.

2 Method

2.1 Numerical Method. It is well established that in the large blood vessels, the blood acts like a Newtonian fluid [35]. The governing equations for the blood flow in the LV are therefore, the 3D, unsteady, incompressible Navier–Stokes equations which are

$$\frac{\partial v_i}{\partial x_i} = 0 \tag{1}$$

$$\frac{\partial v_i}{\partial x_i} + \frac{\partial v_i v_j}{\partial x_j} = -\frac{1}{\rho}\frac{\partial p}{\partial x_i} + \upsilon \frac{\partial^2 v_i}{\partial x_j \partial x_j} \tag{2}$$

where v_i are velocity components in two directions, p is the pressure, and ρ and υ are flow density and kinematic viscosity, respectively.

The equations are discretized in space using a second-order cell-centered, nonstaggered arrangement of the primitive variables v_i and p. A second-order fractional step method is used to integrate the equation in time. The advection term is discretized using a second-order Adams–Bashforth scheme and an implicit Crank–Nicolson scheme is employed to discretize the diffusion term and to eliminate the viscous stability constraint. A geometric multigrid is used to solve the pressure Poisson equation. The boundary conditions on the immersed boundaries are imposed through a sharp-interface IBM, which is well suited for the simulation of complex and moving boundary problems on a Cartesian grid. The details of this flow solver can be found in Ref. [36].

2.2 Left Ventricle Model. A simple model which incorporates the key geometrical features of the LV is employed in the current study. As shown in Fig. 1(*a*), the endocardial surface of the LV is approximated by a prolate-spheroid and the mitral annulus and aorta are represented by two straight tubes which intersect on the top surface of the spheroid. All the dimensions and important geometric parameters are carefully chosen to be within or close to the physiological range, as shown in Table 1, which includes the length of long and short axes, ratio of long and short axes, end diastolic volume, end systolic volume, stroke volume, ejection fraction, mean diameter of mitral orifice, and LV geometric parameter, etc.

The endocardial motion is specified in prior in the current study and the ventricular flow to the LV is driven by this specified motion. During a cardiac cycle, the LV experiences a complex endocardial motion resulting from the nonlinear interaction between the active muscle contraction and ventricular flow. As shown in [37], the complex endocardial motion of the LV can be decomposed into seven simple modes, including an isotropic volume change, twisting, ellipticalization, and four asymmetric modes. Compared with the isotropic volume change, the contribution of other six components is very small (less than 5%) and we neglect them in the current study. Thus, the endocardial surface motion is purely driven by the LV volume change and the ratio of the long axis and short axis is fixed at 2.0 during the whole cardiac cycle [37]. The atrium and aorta are assumed to be fixed in space. The top cap of the model has a circular shape with two circular holes inside, which are the exit of atrium and entrance of aorta. The cap motion is computed by solving the displacement field of a zero thickness membrane using the finite element method with specified displacement boundary conditions. The displacements at two inner holes are enforced to be zero, while the displacement at the outer radius is directly gotten from the specified endocardial motion.

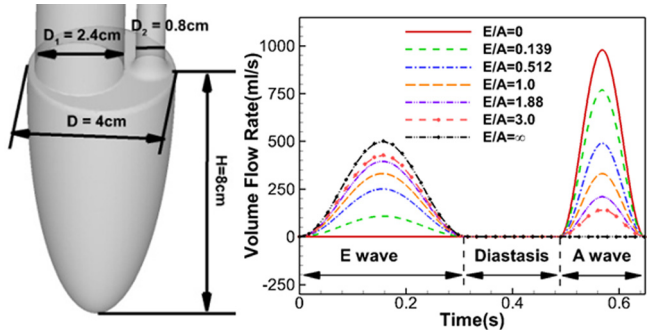

Fig. 1 (*a*) The geometric model of the left ventricle and (*b*) the time history of the ventricular volume flow rate for various cases

Table 1 Comparison of the key geometric and flow parameters of the current model with the physiological range

	Current value	Physiological value
Ratio of long and short axis	2	2.0 [37]
End systolic volume	67 ml	16 ml–143 ml [3]
End diastolic volume	146 ml	65 ml–240 ml [3]
Stroke volume	79 ml	55 ml–100 ml [3]
Ejection fraction	54.1%	55–70% [4]
Diameter of mitral annulus	2.4 cm	2.0 cm–2.5 cm [9]
LV geometry parameters	2.19	1.7–2.0 [19]
E/A ratio	1.88	1.0–2.0 [4]
Vortex formation number	5.7	3.5–5.5 [19]
Heart rate	60 bpm	60 bpm–100 bpm [3]
Cardiac output	4.74 l/min	4.0 l/min–8.0 l/min [3]
Fraction of stroke volume contributed from *A* wave filling	0.21	0.2 [19]

Diastole is composed of three distinct stages: early diastolic filling (*E* wave), diastasis, and late diastolic filling (*A* wave). During the diastasis, the LV volume does not change and the volume flow rate is zero. The volume flow rate of each filling wave in our simulation is represented by a single-frequency sinusoidal wave which is the most energetic wave extracted from a physiological measurement using Fourier transform [15]. The volume flow rate for the entire diastole is described by the following equation:

$$Q(t) = \begin{cases} \dfrac{Q_E}{2}(1-\cos(2\pi f_E t)) & 0 \le t < 0.3125 \\ 0 & 0.3125 \le t < 0.4884 \\ \dfrac{Q_A}{2}(1-\cos(2\pi f_A (t-0.4884))) & 0.4884 \le t < 0.6484 \end{cases} \tag{3}$$

where $Q(t)$ is the volume flow rate, Q_E and Q_A represent the peak volume flow rate of the *E* wave and *A* wave, respectively, with the

value of $Q_E = 393.4$ ml/s and $Q_A = 209.3$ ml/s, f_E and f_A represent the frequency of the E wave and A wave, respectively, with the value of $f_E = 3.2$ Hz and $f_A = 6.25$ Hz. The time history of the volume flow rate is shown in Fig. 1(*b*) corresponding to $E/A = 1.88$. The important key parameters associated with the ventricular flow are well preserved by this volume flow rate. As listed in Table 1, the ejection fraction, E/A ratio, fraction of stroke volume contributed from A wave filling, vortex formation number, heart rate, and cardiac output are well within/close to the physiological range.

It is useful at this stage to point out the potential caveats in the current model. First, the geometric model and wall motion employed for the LV are highly simplified and this simplification will likely affect the LV hemodynamics produced in the simulations. However, past studies have shown that by carefully retaining all of the major geometric parameters and filling parameters, the simplified LV model can reproduce the essential features of cardiac flows [9,10,34]. Simple models also provide us a small cell-defined parametric space to perform parametric studies. Second, the mitral and aortic valves are excluded from the current study. The mitral valve, in particular, can have an important effect on the filling flow patterns [27,38]. However, the choice of an appropriate inflow profile coupled with a matching vortex formation number can alleviate some of this discrepancy, etc. [19]. Third, the trabeculae in the inner LV walls and the papillary muscles are excluded in the model by assuming a smooth-walled endocardium. These features might enhance mixing and viscous dissipation in the LV. However, including these details will significantly increase the modeling and computational effort.

2.3 Simulation Setup. The entire model is immersed into a 5.28 cm × 5.28 cm × 16 cm rectangular computational domain. A high resolution of 128 × 128 × 256 Cartesian grid is employed in the computational domain in order to resolve the complex flow in the ventricle and a small time-step corresponding to 0.02 ms is employed. Thus, the entire diastole phase of 0.6484 s requires 32,420 time steps. During the computation, a zero-velocity-zero-pressure-gradient wall boundary condition is applied at the exit of the aorta to mimic the blockage of the aortic passage and a zero-velocity-gradient-zero-pressure inflow boundary condition is applied at the entrance of the atrium to allow the flow to enter the ventricle through the mitral annulus.

As aforementioned, the LVDD is usually manifested by an abnormal E/A ratio while the ejection fraction is well preserved. For the normal subject, the E/A ratio is usually between 1 and 2. For impaired relaxation associated with early-stage DD, the E/A ratio could drop to less than one, and it will get back to the normal range when "peudonormalization" occurs and becomes greater than 2.0 for even more severe dysfunction. In the current study, the E/A ratio is chosen in a wide range from 0.0 to ∞ by changing Q_E and Q_A to cover all the stages of DD. The chosen E/A ratios are showing in Table 2, and the case corresponding to $E/A = 1.88$ is considered as the normal filling case. Other parameters, including the periods of E and A waves, stroke volume, end systolic volume as well as systolic volume flow rate are kept same among all the cases. The resulted ventricular volume flow rate for all the cases is plotted in Fig. 1(*b*) and the peak volume flow rate for the E wave and A wave (Q_E and Q_A) for various cases is listed in Table 2. The variation of the E/A ratio also results in the variation of the fraction of stroke volume due to A wave (β) [19] and the vortex formation time for E wave and A wave (Γ_E, Γ_A) [19], which are also listed in Table 2. The Reynolds numbers are also computed and listed for the E wave and A wave separately based on the maximum filling velocity and diameter of the mitral office which are in the same range of other recent studies [9]. The effects of E/A ratio on vortex dynamics, flow propagation speed, energy consumption as well as flow transport and mixing are discussed in Sec. 3.

Table 2 The *E/A* ratio, the fraction of stroke volume due to *A* wave (β), peak volume flow rate (Q_E, Q_A), vortex formation time (Γ_E, Γ_A), and Reynolds number (Re_E, Re_A) for the *E* and *A* waves for various cases. Reynolds number is defined as $Re = U_{max}D_1/\upsilon$, where U_{max} is the maximum filling velocity through the mitral inlet. The vortex formation time is defined as $\Gamma = V/(\pi D_1^3/4)$, where *V* is the filling volume of each wave.

E/A	β	Q_E (ml/s)	Q_A (ml/s)	Γ_E	Γ_A	Re_E	Re_A
0.0	1.0	0.0	977.3	0.0	7.22	0.0	1720
0.129	0.79	107.1	768.1	1.52	5.7	194	1340
0.512	0.5	250.3	488.6	3.61	3.61	474	856
1.0	0.34	331.4	330.9	4.77	2.45	633	551
1.88	0.21	393.4	209.3	5.7	1.52	754	371
3.0	0.146	427.6	142.5	6.17	1.05	819	259
∞	0.0	500.6	0.0	7.22	0.0	959	0

3 Result and Discussion

3.1 Vortex Dynamics. Figure 2 shows a sequence of instantaneous snapshots of 3D vortical structures at eight time instants over the entire diastole phase for the normal filling case ($E/A = 1.88$). The vortical structure is visualized by using the isosurface of eigenvalue of velocity gradient. It reveals that the diastolic flow in a normal LV is primarily characterized by the formation and evolution of a series of vortex rings.

At the initial phase of the early filling (Fig. 2(*a*)), a large well-defined vortex ring (R1) is formed at the exit of the mitral orifice as a result of the shear layer roll up of the filling jet. Owing to the eccentric location of the mitral orifice, R1 is inclined and asymmetric. As the vorticity from the boundary layer of the filling jet continuously flows into R1, R1 continuously grows in size both radially and axially while it convects downward, as seen in Fig. 2(*b*). Shortly afterward, as seen in Figs. 2(*c*) and 2(*d*), the left (posterior) side of R1 impinges on the lateral wall of the LV and starts to break down to small-scale structures due to strong

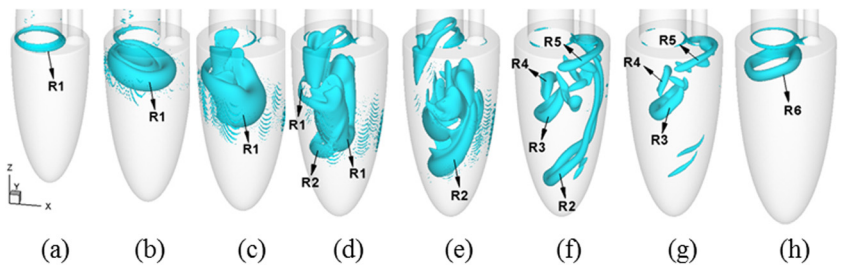

Fig. 2 The time evolution of the vortical structure during the diastole phase for the normal filling case ($E/A = 1.88$). The vortical structure is visualized by using the eigenvalue of velocity gradient. (*a*) $t = 0.06T$, (*b*) $t = 0.156T$, (*c*) $t = 0.22T$, (*d*) $t = 0.272T$, (*e*) $t = 0.316T$, (*f*) $t = 0.448T$, (*g*) $t = 0.488T$, and (*h*) $t = 0.648T$. *T* is the time for one cardiac cycle. $T = 1$ s.

ring–wall interactions. In the meanwhile, the vorticity from the boundary layer of the filling jet continues to flow into the right (anterior) side of R1, leading to even faster growth of this portion. It should be noted that the right (anterior) portion of R1 is now growing aligned with the axis of the ventricle; as its left (posterior) portion stays on the original plane, the entire R1 now resides on two planes at an angle. Moreover, some vorticity reconnection between the inner-race of R1 and interior surface of the LA is observed in the form of a pair of secondary vortex tubes. It is worth noting that the complex 3D topology of R1 as well as the secondary vortex tubes observed in our simulations has also been observed in many other past studies where either simplified or patient-specific LV models were used [9,29]. As we carefully examine the vorticity field, it is evidenced that the occurrence of the secondary vortex tubes is a direct result of the interaction between the left (posterior) side of R1 and the ventricular wall. The structure and evolution of R1 are closely related to the vortex formation time, which is defined as $V/(\pi D^3/4)$, where V is the filling volume and D is the diameter of mitral orifice [19]. According to Gharib et al. [18], the leading vortex ring pinches off from the trailing jet with its maximum circulation when the formation time beyond the critical value which lies in the range of 3.6–4.5. For the current normal filling case, the formation time of the E wave is 5.7. Thus, at the end of the E wave, as seen in Fig. 2(*e*), the entire ring-shape structure of R1 has completely disappeared and broken down into small-scale structures. It suggests the significant dissipation of R1 occurs during the late E wave phase, which is believed due to the decreased intensity of R1 after its pinch-off as well as the increased 3D instability induced by the strong wall–ring interactions.

In addition to R1, it is of great interest to notice the formation of another vortex ring, R2, during the late E wave phase (Figs. 2(*d*) and 2(*e*)). Same as the afore-observed vortex tubes, R2 is also a direct consequence of the ring–wall interactions; however, in contrast to the vortex tubes, the interaction occurs between the right (anterior) portion of R1 and ventricular wall. In Fig. 2(*d*), R2 clearly shows a ring-shape structure with one end attached to the bottom of the right (anterior) portion of R1. While R1 is quickly dissipated in Fig. 2(*e*), R2 rapidly grows and expands with the left (posterior) side moving toward the apex and the right (anterior) side advancing upward toward the aorta. At the end of the E wave (Fig. 2(*e*)), it forms an elongated shape to fill up the central cavity of the ventricle. During the diastasis, as seen in Fig. 2(*f*), most vortical structures generated during the E wave are dissipated. Interestingly, the remnant of R1, however, evolves into two new vortex rings, R3 and R4, in the upper part of the ventricle. Moreover, R2 moves closer to the septal wall and is further stretched along the long axial direction so that it almost fills up the elongated shape of the entire ventricle. The upper side of R2 interacts with the septum adjacent to the aortic entrance to form a small ring that surrounds the aorta, which is R5. At the end of the diastasis, in Fig. 2(*g*), R2 almost completely disappeared due to the strong dissipations while R3, R4, and R5 reside to continuously interact with the late filling jet. During the late filling (Fig. 2(*h*)), another weaker vortex ring, R6, is generated. Since the vortex formation time is 1.56, R6 does not fully pinch-off from the filling jet. It is generally confirmed by the past work that the diastolic vortex ring creates large rotational flows in the central cavity of the LV, which has a functional advantage that it redirects the inflow from the atrium toward the aorta and thereby reduces the work that would have to be done by the ventricle during the systole to eject a certain volume of blood. To illustrate this feature, in Fig. 3, we plot the velocity vectors and 3D swirl strength contours at the midaxial plane of the LV for the normal filling case at three time instants, which are at the late E-wave, end E-wave, and end A-wave, respectively. For the sake of clarity, the velocity vectors are shown every five other points in both X and Z directions. At the late E wave (Fig. 3(*a*)), one can clearly see that the strong vortex ring R1 generates a counter-clockwise circulation of the flow in the central cavity of the ventricle; the

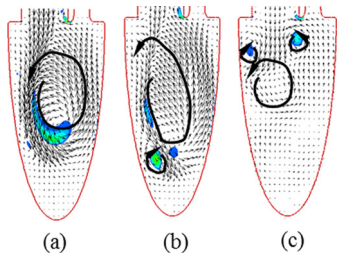

Fig. 3 The velocity vectors and 3D swirl strength at the midaxial plane at three time instants. (*a*) $t = 0.272T$, (*b*) $t = 0.316T$, and (*c*) $t = 0.648T$.

blood flow at the lateral wall side primarily goes down to the apex, while the flow adjacent to the septal wall moves up toward the aorta. Swirl strength indicates the existence of the weak vortex ring, R2, near the lateral wall. At this instant, the apex region remains unaffected by the inflow. Swirl strength in Fig. 3(*b*) indicates the strong dissipation of R1 and quick intensification of R2 at the end of the E wave. R2 moves closer to the near-apex region and generates a clockwise circulation there. Interestingly, despite the significant deformation and strong dissipation of R1, the big counter-clockwise circulation initially generated by R1 persists during the entire diastole. At the end of the A wave (Fig. 3(*c*)), this big rotational flow pattern still remains in the central cavity of the ventricle to continuously support the redirection of the blood flow toward the aorta during the systole, although its strength is significantly weakened.

While the diastolic vortex ring (R1) is a common observation confirmed by recent in-vivo MRI measurement and other computational fluid dynamics (CFD) models [9,21,29,39,40], the existence of R2 is a new finding of the current study. From the function aspect, R2 is believed to play an important role in terms of maintaining high filling velocity and mixing. Previous work [41,42] hypothesized that the diastolic vortex ring creates a virtual hydrodynamic channel extending from the mitral valve toward the apex of the heart. This channel has a functional advantage that it prevents the spreading and momentum loss of the filling jet so that high filling velocity is maintained. In the current study, we further hypothesize that the formation of R2 extends this hydrodynamic channel and allows the blood continuously moving with a high filling velocity from the LV inflow tract to the apex during late E wave. The presence of the vortex ring also promotes the mixing of the ventricle blood and fresh atrium blood by entraining the ambient fluid into the ring (this point will be discussed in detail in Sec. 3.4). From this aspect, R2 is also very important to continuously washout the near-apex region and enhances the mixing of the apex blood with the incoming flow.

To illustrate the effects of changing E/A ratio on diastolic vortical structures, Fig. 4 plots the isosurface of eigenvalue of velocity gradient at five different time instants for the case $E/A = 0.129$. Since the E wave is significantly weaker than the A wave for this

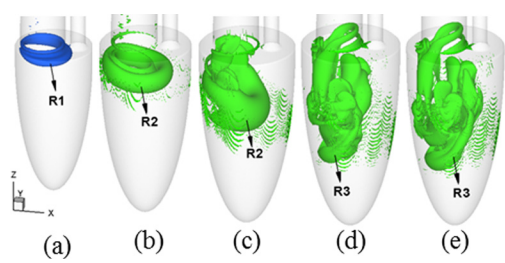

Fig. 4 The time evolution of the vortical structure during the diastole phase for the case with $E/A = 0.129$. The vortical structure is visualized by using the eigenvalue of velocity gradient. (*a*) $t = 0.156T$, (*b*) $t = 0.568T$, (*c*) $t = 0.604T$, (*d*) $t = 0.64T$, and (*e*) $t = 0.668T$.

case, to clearly depict the vortical structure, we choose the isosurface value to be half and double of the value plotted in the normal case (shown in Fig. 2) for the *E* wave and *A* wave, respectively. For two reasons, we choose this case: First, it has a very low *E*/*A* ratio which could represent a severe impaired relaxation condition, so significant changes in the vortical structure are expected; second, the vortex formation time for this case is 1.52 and 5.7 for the *E* wave and *A* wave, respectively, which is the exact opposite to the normal filling case, so the effect of the vortex formation time can be eliminated when cross compare the *E* wave and *A* wave vortical structures for two cases. At the first glance, it seems that the overall evolution of the vortical structure for this case is very different from the normal filling case; however, a more careful examination reveals that the key features of the basic vortical structure are essentially same for two cases but appear in different filling phases. Under the diseased condition, the *E* wave jet creates a weak vortex ring, R1 (Fig. 4(*a*)), which is also asymmetric and inclined as it convects toward the apex. With a formation time of 1.52, R1 is not able to pinch-off from the filling jet and stays near the mitral inlet entrance with very little interaction with the ventricular wall during the entire *E* wave. Then, R1 quickly dissipates during the diastasis and completely disappears before the *A* wave starts. The *A* wave jet, on the other hand, with the same vortex formation time as the *E* wave jet in the normal filling case, presents similar development of the vortical structures to that wave.

Figures 4(*b*)–4(*e*) shows that the *A* wave vortical structures are characterized by the formation and development of two vortex rings, R2 and R3, corresponding to R1 and R2 in Figs. 2(*d*)–2(*e*). Strong vortex tubes extending into the mitral orifice are also observed. These complex vortical structures will remain in the ventricle before the systole starts.

As we examine all of the simulated cases, two common features associated with the filling process are observed. First, two distinct vortex topologies are found associated with the strong and weak fillings, respectively. The strong filling is characterized by a complex vortical evolution of two primary vortex rings, as R1 and R2 in Fig. 2, into three small vortex structures, as R3, R4, and R5 in Fig. 2. The weak filling is characterized by a single weak vortex ring, as R6 in Fig. 2. The underlying vortex structures are determined by the combined effects of the vortex formation number and the flow propagation speed (the calculation and detailed discussion on flow propagation speed is provided in Sec. 3.2). Figure 5 plots the flow propagation speed against the vortex formation time for both *E* wave and *A* wave of all the simulated cases. We have highlighted the region with the grey color, where all the waves located inside are strong fillings. It is found that the strong fillings occur during the *E* waves when $E/A > 1$ and *A* waves when $E/A < 1$, for which the vortex formation time is greater than 3.6 and the flow propagation speed is greater than 32 cm/s. For the case $E/A = 0.512$, the *E* wave and *A* wave share

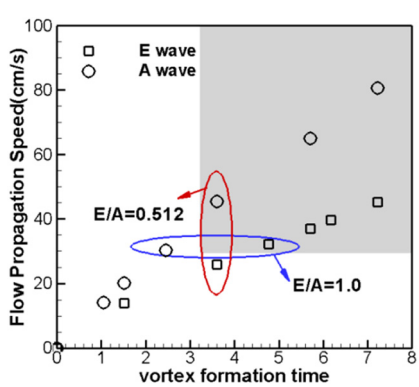

Fig. 5 The flow propagation speed versus the vortex formation time for each *E* wave and *A* wave of all the cases. Grey region represents the "strong" filling waves associated with complex vortical structures.

the same vortex formation time of 3.61. However, the strong filling occurs during the *A* wave for which the flow propagation speed is 45.49 cm/s. For the case $E/A = 1$, the flow propagation speed is nearly same for the *E* wave and *A* wave, however, the vortex formation time during the *E* wave ($\Gamma_E = 4.77$) is much higher than the *A* wave ($\Gamma_A = 2.45$) and the strong filling occurs during the *E* wave. Therefore, we hypothesize that the strong filling characterized by the complex ventricular vortical structures is triggered when both vortex formation time and flow propagation speed are high, which need to be greater than 3.6 and 32.28 cm/s, respectively, in our cases. In fact, the complex evolution of vortex structures during the strong filling is the direct result of the vortex–wall interaction. With a high vortex formation time and flow propagation speed, the vortex ring (R1) is able to pinch-off from the filling jet and quickly convect downward to interact with the ventricular wall. A low vortex formation time will cause the vortex ring to stay near the mitral inlet without pinch-off and a low flow propagation speed causes a very low convection speed of the vortex ring which may have fully dissipated before it meets the ventricular wall. It should be noted that due to our sparse data, the critical vortex formation time and flow propagation speed does not need to be exactly same as our simulation cases, they could be anywhere between 2.45–3.61 and 25 cm/s–32 cm/s, respectively.

Second, there is very little connection in vortex structures between the two filling phases. In our cases, even with a strong *E* wave, some remnant vortices from the *E* wave are observed during the *A* wave, they are very weak and have little influence on the *A* wave vortex. This weak intercardiac phase connection is because the vortex structures of the early filling have decayed during the long diastasis period. Thus, according to the above, if the diastasis is long enough, changing *E*/*A* ratio only changes the emerging sequence and strength of these two types of distinct vortical structures. However, it should be noted that for some diseased cases, such as high heart rate in which the diastasis becomes shorter, or dilated LV, the vortex structures may not have sufficient time to dissipate through the diastasis. In these cases, the *E* wave structures will affect the *A* wave structures. Nevertheless, our observations that there is little connection of fluid dynamics between the *E* wave and *A* wave which provides an evidence to the assumption that the diastolic early filling and late filling can be investigated separately in the cases with a relative long diastasis, which have also been widely adopted in the past studies [9,14,29].

3.2 Flow Propagation Speed. As observed by past in-vivo measurements [4], the maximum filling velocity has high intersubject variations and high sensitivity to the preload situations, making it hard to provide a universal criterion to assess the ventricular filling function. In contrast, the flow propagation velocity, which is commonly estimated by the color M-mode Doppler endocardiogram in the medical practice, has been proved to be insensitive to intersubject difference as well as the preloads, therefore is frequently used to evaluate the LV diastolic performance [5]. In the current study, the "virtual" color M-mode Doppler endocardiogram along the axis of the mitral orifice is constructed from the CFD simulation data by plotting the contours of the normal filling velocity in the space of time and distance to the apex. The flow propagation velocity is computed by the slope of the first 50% isovelocity contour line of the maximum filling velocities. Figure 6(*a*) depicts the "virtual" M-mode for the normal filling case, and the flow propagation velocities are calculated to be 37.1 cm/s and 20.2 cm/s for the *E* wave and *A* wave, respectively. The physiological range of the *E* wave flow propagation velocity is 37 ± 13 cm/s as reported by Carcia et al. [5]; therefore, the simulated value is well within the physiological range.

The flow propagation speed for both *E* wave and *A* wave for all the cases is computed and plotted against the corresponding peak volume flow rate in Fig. 6(*b*). It is interestingly noticed that the flow propagation speed linearly scales up with the peak volume flow rate and two slopes associated with the *E* and *A* waves are

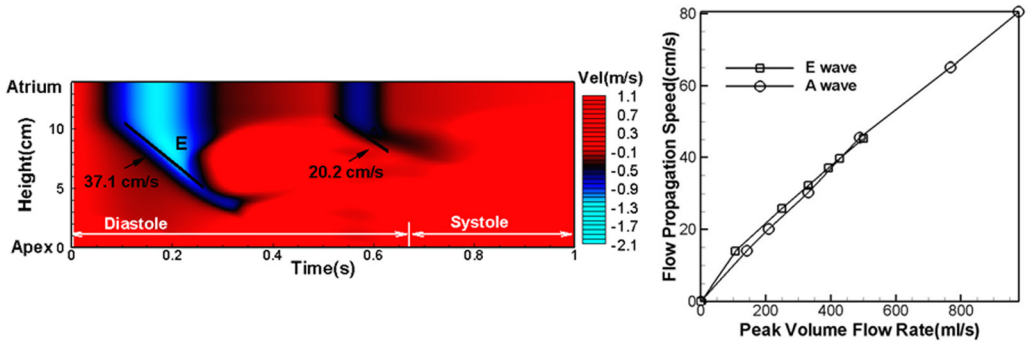

Fig. 6 (*a*) A spatiotemporal contour of the flow velocity along the long axis for the normal filling. (*b*) The variations of the flow propagation speeds with vortex formation number for the *E* wave and *A* wave.

nearly identical, which is about 0.082 cm/ml. It clearly indicates that the velocity propagation speed is determined by the peak flow rate and is insensitive to other conditions, such as the filling period, different filling phases, etc. A decrease in the propagation speed is an indication of a reduced suction function of the LV.

3.3 Energetics. The effect of abnormal *E/A* ratios on the energetic of the LV filling was also explored. Considering the LV as a control volume system, the total energy of the system is constituted of five components, which are the incoming kinetic energy (KE_{in}) and flow work (W_f) of mitral inflow, pressure work by the ventricular wall on the flow (W_p), total kinetic energy change (ΔKE), and viscous dissipation inside the ventricle (Φ). The time rate of changes of each energy component is calculated as follows:

$$\dot{KE}_{in} = -\int_{S_m} \frac{1}{2}\rho_0 |\vec{u}|^2 \vec{u}\cdot\vec{n}_m dS, \quad \dot{W}_f = -\int_{S_m} p\vec{u}\cdot\vec{n}_m dS,$$

$$\dot{W}_p = -\int_{S_e} p\vec{u}\cdot\vec{n}_e dS$$

$$\Delta\dot{KE} = \frac{d\int_V \frac{1}{2}\rho_0 |\vec{u}|^2 dV}{dt}, \quad \dot{\Phi} = \int_V (\tau : \nabla\vec{u}) dV$$

where S_m and S_e are the area of the mitral inlet and endocardial surface, respectively, n_m and n_e are the surface normal unit vectors on those surfaces, V is the ventricular volume, ρ_0 is the blood density, $\vec{u}$ is the blood velocity, τ is the viscous stress, and $\nabla\vec{u}$ is the deformation tensor. Conservation of the total energy requires $\Delta\dot{KE} + \dot{\Phi} - \dot{KE}_{in} - \dot{W}_f - \dot{W}_p = 0$. Figure 7(*a*) shows the instantaneous time rate of changes of these five quantities during the diastole in the normal filling case. At each time instant, the overall energy balance has been carefully checked to be zero to confirm the conservation of the total energy. The time history of the volume flow rate is also superimposed to clearly visualize different phases. As illustrated in Fig. 7(*a*), the incoming kinetic energy flux ($\dot{KE}_{in}$) associated with the mitral inflow is completely in phase with the volume flow rate. The flow work ($\dot{W}_f$), however, oscillates sinusoidally during each filling phase with a higher negative peak during the inflow acceleration and a lower positive peak during the inflow deceleration. The pressure work ($\dot{W}_p$), interestingly, presents roughly similar behavior with the flow work, but with an opposite sign. These patterns of both flow work and pressure work are found directly associated with the pressure time variation inside the LV. Figure 8(*a*) shows the time variation of volume-averaged pressure inside the LV superimposed by the volume flow rate. The averaged LV pressure exhibits an asymmetric double peak pattern with a higher negative peak during the inflow acceleration and a lower positive peak during the inflow deceleration. Negative LV pressure sucks the blood in and yields a positive pressure work from the ventricular wall and a negative flow work from the mitral inflow on the LV control system; positive pressure has the opposite effect vice versa. It should be noted that the averaged pressure is directly associated with the overall inflow acceleration. Figure 8(*b*) plots the magnitude of the peak averaged pressure during the acceleration and deceleration for both *E* wave and *A* wave versus the amplitude of inflow acceleration, which is the product of the peak volume flow rate and filling frequency for each case. We noticed that the peak averaged pressure is linearly scaled up with the amplitude of flow acceleration, and this linear scaling has two different slopes according to the flow acceleration phase and deceleration phase. The slope is steeper in the flow acceleration phase, which is consistent with our previous observation that higher pressure peak occurs during

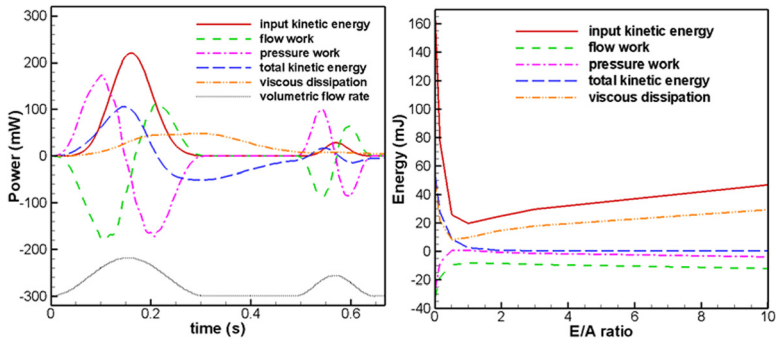

Fig. 7 (*a*) The instantaneous time rate of the changes of five energetics components of the normal case (*E/A* = 1.88) during the diastole. The volume flow rate is superimposed at the bottom. (*b*) The total energy of five components during the diastole versus *E/A* ratio.

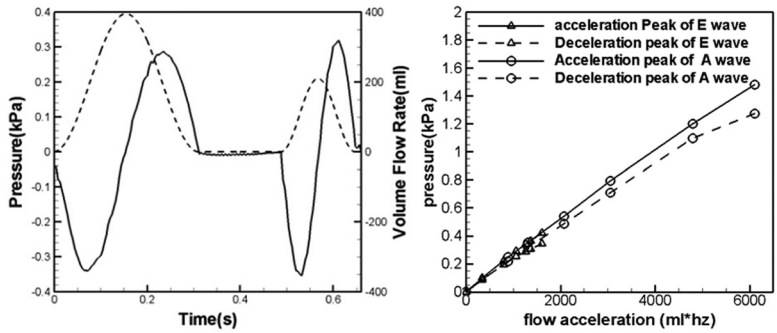

Fig. 8 (*a*) The time variation of the volume-averaged pressure inside the LV for the normal filling case; (*b*) the magnitude of the peak averaged pressure during the acceleration and deceleration for both *E* wave and *A* wave versus the amplitude of inflow acceleration

the flow acceleration phase. The linear relation between the peak averaged pressure and amplitude of flow acceleration is a common observation in inviscid flows, and here different slopes are due to viscous effects. Viscous dissipation impedes flow acceleration and facilitates flow deceleration. According to the NS equation, in order to achieve the symmetric flow acceleration and deceleration, the pressure gradient in the flow acceleration phase must be higher than that in the flow deceleration phase. Therefore, with the constant pressure on the mitral inlet, the pressure peak during the flow acceleration phase needs to be higher than that during the deceleration phase.

The time rate of the total kinetic energy change initially follows the trend of the incoming kinetic energy flux that it goes up during the inflow acceleration and goes down during the flow deceleration. However, as we discussed previously, toward the end of early filling, the primary vortex ring (R1 in Fig. 2) significantly dissipates and breaks down to small-scale structures, which will greatly enhance viscous dissipations. As a result, the time rate of the total kinetic energy change quickly goes down to negative values toward the end of *E* wave and continues to be negative throughout the diastasis until another small increase due to the *A* wave filling. The great enhancement of the viscous dissipation during the late *E* wave and diastasis is also reflected in the viscous dissipation curve in Fig. 7(*a*).

To quantify and examine the total changes of each energy component throughout the entire diastole for various cases with different *E*/*A* ratios, we integrate the time rate of changes of each quantity over the diastole and plot them versus the *E*/*A* ratio in Fig. 7(*b*). In order to make the plot readable, we use $E/A = 10$ to represent the case $E/A =$ infinity. We have several observations through these plots. First, the incoming kinetic energy is the most dominant term in the overall energy budget. It reaches its minimum value at $E/A = 1$. When the *E*/*A* ratio is less than 1, the incoming kinetic energy increases dramatically with the decrease in *E*/*A* ratio, while when the *E*/*A* ratio is greater than 1, the incoming kinetic energy increases very mildly with the increase in *E*/*A* ratio. Interestingly, the viscous dissipation curve is almost parallel to the incoming kinetic energy curve, indicating that the viscous dissipation is mostly dependent on the incoming kinetic energy. However, the minimum viscous dissipation occurs at $E/A = 0.5$. In addition, the pressure work also reaches its minimum value at $E/A = 0.5$, which suggests the minimum ventricular work needed to suck the same amount of the blood. According to the above, we hypothesize that the optimal range for *E*/*A* ratio in terms of energy consumption is 0.5–2 under the flow condition investigated. In the healthy heat where the *E*/*A* ratio is between 1 and 2, the heart maintains an optimal blood transport by minimizing the kinetic energy input, viscous dissipation and required work. Second, all energy compositions increase quickly when the *E*/*A* ratio is less than 0.5, which could be associated with severe impaired relaxation. In this case, both ventricle (pressure work) and atrium (input kinetic energy) are required to work harder to maintain the pump performance (ejection fraction). However, through the remodeling process, the heart starts to adapt and move back to its normal energy range to maintain the minimum energy consumption (pseudonormalization). Even in the late stage of DD in which the *E*/*A* ratio is greater than 2, the energy consumption only increases slightly. Thus, we hypothesize that one of the possible aspects of heart remodeling is that the heart is trying to maintain its optimal energy consumption.

3.4 Blood Mixing and Transport. The mixing and transport of the atrial and ventricular blood cells are other physiologically important characteristics of LV performance since it determines the composition of the ejected blood as well as the residence time of the blood cells in the LV. The degree of the mixing as well as the pattern of the atrial and ventricular blood at the time of ejection depends on intraventricular flow dynamics. While it is generally assumed a complete mixing in the healthy LV, diseased LV usually generates very different flow patterns which would be expected to reduce the mixing.

In order to explore the effects of *E*/*A* ratio on blood flow mixing and transport, we employed the scalar transport equation to describe the transfer of the blood cells inside the LV during the diastole for various cases. At the beginning of the diastole, the LV is full of residual blood cells from the previous cycle and we tag them as the "ventricular" blood cells. During the filling, the fresh blood enters the LV and we tag them as the "atrial" blood cells. Two scalars, φ_1 and φ_2, are defined to represent the volume concentration of the "ventricular" blood cells and "atrial" blood cells, respectively. Therefore, φ_1 is 1 everywhere inside the LV at the beginning of the diastole, φ_2 is 1 inside the atrium during the filling and $\varphi_1 + \varphi_2 = 1$ everywhere throughout the entire diastole phase. These two scalars are transported by the Eulerian velocity field obtained from the flow simulation and computed by solving the scalar transport equation on the same computational mesh using the immersed-boundary method. A zero flux boundary condition is given at the myocardium wall.

In order to demonstrate the transport and mixing of the two groups of blood cells in the ventricle, we plot contours of φ_2 on the center plane of the LV at five time instances during the diastole for the normal filling case ($E/A = 1.88$) and the case with $E/A = 0.129$, respectively, in Fig. 9. During the diastole, blood mixing is mainly dominated by two mechanisms: shear layer entrainment of the vortex ring and the complex flow pattern transport after vortex ring breakdown. As seen in Fig. 9(*a*) for the normal filling case, during the *E* wave jet ejection, the shear layer

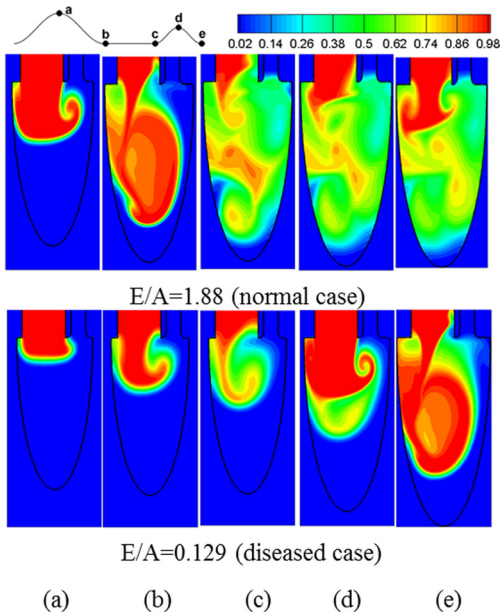

Fig. 9 The contour of the volume content of the atrial blood inside the LV at five instants during one cycle. (*a*) $t = 0.152T_E$, (*b*) $t = 0.316T$, (*c*) $t = 0.488T$, (*d*) $t = 0.568T$, and (*e*) $t = 0.648T$. The first row is from the normal case ($E/A = 1.88$) and the second raw is from the diseased case ($E/A = 0.129$).

which separates from the tip of the mitral inlet rolls up and entrains the ambient ventricular blood into the forming vortex ring, R1 in Fig. 2(*a*). As this vortex, ring grows in size and convects downward, more ventricular blood is entrained into the ring. These ventricular blood cells continue to convect to the core region of the vortex ring and mix with the atrial blood there, as seen in Fig. 9(*b*). Since the entrained ventricular blood is much less than the ejected atrial blood, the volume content of the ventricular blood inside the vortex rings is very low. It is also noticed that during the entire *E* wave ejection phase, the ventricular blood external to the vortex ring remains nearly unaffected. Thus, the effect of shear entrainment of vortex ring on the flow mixing is generally small. This has been confirmed by the previous experimental studies as well [43]. During the diastasis, the *E* wave vortical structures break down to small eddies and the intraventricular flow becomes highly complex. Consequently, two groups of blood quickly mix up inside the whole ventricle during this stage. In the meanwhile, the big counter-clockwise circulation inside the ventricle will also enhance the mixing. At the end of the diastasis, i.e., as shown in Fig. 9(*c*), they are more uniformly mixed in the LV with a small concentration fluctuation. Blood mixing during the *A* wave is dominated by the vortex ring entrainment again. During jet ejection (Figs. 9(*d*) and 9(*e*)), the formed vortex rings entrain the ambient fluid to the core region of the ring. The incoming kinetic energy during the *A* wave is much smaller than the *E* wave therefore, the entrainment is not as strong as in the *E* wave. It only affects the region close to the mitral inlet. Throughout the entire diastole, the mixing level in the apex region is very low, indicating that the ejected atrial blood does not have enough kinetic energy to reach the apex region. It can be found for this case that the complex flow pattern induced by the vortex ring breakdown induces much stronger mixing than the shear layer entrainment of the vortex ring. It is interesting to note that the topological structure of blood transportation and mixing is captured using Lagrangian Coherent Structure on the PCMRI and Echo measurements are also found characterized by the vortex ring and the resulting large circulation in the center of the ventricle [44,45]. The diseased case with $E/A = 0.129$ presents completely different mixing patterns from the normal case. The flow patterns which should have been generated after the breakdown of the *E* wave vortical structures become very simple due to the significantly reduced momentum of the *E* wave jet; therefore, the blood mixing is primarily induced by ambient fluid entrainment of the shear layers of vortex rings, and it is only found at the core region of the formed vortex ring. However, a strong blood mixing should be expected during the systole after the *A* wave structures breaks down to small eddies.

In order to quantify the mixing quality inside the LV for various cases, we define a standard deviation of the atrial blood concentration from perfect mixing, std, which is given by

$$\text{std} = \sqrt{\frac{1}{N}\sum_{i=1}^{N}(\varphi_{2_i} - \text{EF})^2}$$

where N is the number of computational cells. By definition, if two groups of blood are perfectly mixed, φ_2 should be equal to *EF* everywhere inside the LV. Therefore, std shows how much variation of mixing of two groups of blood forms perfect mixing. A lower value of std indicates a higher mixing level, and $\text{std} = 0$ indicates perfect mixing everywhere inside the LV.

Figure 10 shows std at the end-diastole versus various *E*/*A* ratios. For the normal filling case, $\text{std} = 0.18$, indicating that even the healthy heart cannot achieve perfect mixing in the LV. std monotonously decreases with the increase in the *E*/*A* ratio except when $E/A = 0$. This feature is consistent with the findings from Fig. 9 that a stronger *E* wave leads to a more complex flow pattern which greatly enhances the blood mixing during the diastasis. On the other hand, the reversed *E*/*A* ratios which might be emerging from impaired relaxation reduce blood mixing quickly.

In order to provide spatial information about the blood mixing inside the LV, we define another index to quantify the volume of the stagnation region inside the LV. For the healthy heart, it is ideal that the whole LV is completely flushed by the atrial blood after each cycle so that the old blood cells inside the LV can be replaced by the freshly oxygenated blood cells. We compute the volume percentage of the stagnation region at the time of end-diastole and present them in Fig. 10. The stagnation region is defined as the area where φ_2 is less that 5%. It is shown that when $E/A > 1.0$, the volume of the stagnation region is almost zero. However, as the *E*/*A* ratio drops below 1.0, the stagnation area increases very fast. The highest value, which is as high as 15%, appears in the case of $E/A = 0.129$. It suggests that early diastolic dysfunction might increase the risk of blood clot while in the late stage of DD, the entire ventricle is able to be flushed by the atrial blood.

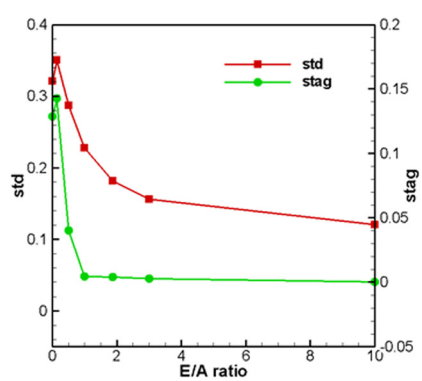

Fig. 10 The variations of the standard deviation of the volume content of the atrial blood from the EF (std) and the volume percentage of the stagnation region inside the LV (stag) with the varying *E*/*A* ratio

4 Conclusion

Three-dimensional numerical simulations are employed to investigate the hemodynamic effects of abnormal *E/A* ratios on LV filling function. In this study, the endocardial surface of the LV is represented by a prolate-spheroidal geometry and the wall motion is driven by a prescribed ventricular volume change which consists of the early (*E*) and atrial (*A*) filling stages. The simulations are carried out with an accurate parallelized immersed-boundary flow solver which allows us to simulate this flow on a stationary Cartesian grid. A wide range of *E/A* ratio from 0 to infinity is employed with the aim to characterize the stages of impaired relaxation associated early DD, pseudonormalization, and restrict filling. It should be noted that *E/A* ratio is just one of the diagnostics criteria of stages of LVDD and this ratio should not be confused with the condition itself. While our study is able to confirm some common findings reported by previous studies, the simulations have also uncovered some interesting new features presented below:

(1) Under the normal filling condition, the early filling flow pattern is characterized by two vortex rings. While the first ring is the leading vortex ring of the filling jet responsible for maintaining the high filling velocity and generating large rotational flow in the central cavity, the second ring emerges as the result of interactions between the ventricular wall and the leading vortex ring, primarily responsible for extending the hydrodynamic channel for filling and blood mixing near the apex region.
(2) Changing *E/A* ratio does not change the basic vortical structures, since they are observed to be same among all the cases. However, changing *E/A* ratio does change the emerging sequence and strength of these vortical structures. The vortical structure is resulted by the vortex–wall interaction which is dominated by both vortex formation time and flow propagation speed. A stronger filling is characterized by very complex vortical evolution of a series of vortex rings and their breakdown, and a weaker filling is represented solely by a weak vortex ring.
(3) The vortical structures in two filling phases have very little connection. This supports the assumption that the diastolic early filling and late filling can be investigated separately in terms of fluid dynamics.
(4) The flow propagation speed is found to be linearly scaled up with the peak volume flow rate for both early filling and late filling phases. Other factors, such as the filling period, filling phase, do not change the flow propagation speed.
(5) The optimal range for *E/A* ratio in terms of the energy consumption is 0.5 to 2 under the flow condition investigated. Within this range, the LV requires lowest kinetic energy input and ventricular pressure work and causes smallest viscous dissipation to maintain the normal EF. The cases with $E/A < 0.5$ which could be associated with the severe impaired relaxation are found to consume more energy. The cases with $E/A > 2$, which could be associated with the pseudonormalization and late stage of DD, are found to restore the optimal energy consumptions.
(6) The volume-averaged LV pressure presents an asymmetric double peak pattern during the diastole. The asymmetry is resulting from the viscous effects. The peak volume-averaged LV pressure was found to linearly scale up with the amplitude of the forcing term, and the scaling slopes are associated with the inflow acceleration and deceleration despite of filling phases.
(7) The blood mixing inside the LV is found to be driven by two mechanisms: shear layer entrainment of the vortex ring and the complex flow pattern transport after vortex ring breakdown. The effect of turbulent transport is dominant. Decreasing *E/A* ratio significantly reduces the mixing level in the LV during the diastole and increase the area of stagnation due to reduced flow complexity during the diastasis. There is almost no stagnation region in the healthy heart as well as the diseased heart with restrictive filling.

It is important to reiterate the limitations of this study which include the simplicity of ventricle geometry and motion, the exclusion of mitral valve, and symmetric wave form of the filling volume flow rate. These simplifications could potentially produce differences from the real flow. It also should note that there are numerous factors that cause diastolic dysfunction, such as LV hypertrophy, LV dilatation, pericarditis, etc. Each single pathological condition could yield differences in terms of hemodynamics and blood mixing. However, one common feature of diastolic dysfunction disregarding the genesis is the abnormal *E/A* ratio. From a fluid mechanics point of view, the abnormal *E/A* ratio is associated with the abnormal pressure drop from the LA to the LV during filling phases even though the abnormal pressure drop could originate from a variety of pathological conditions. The ventricular filling function in the LV is primarily determined by the pressure drop. Thus, there is a direct connection between the abnormal *E/A* ratio and filling function and this connection may be general for different types of diastolic heart dysfunction. The current study aims to disclose this underlying connection by using a simple model. Patient-specific model with a high level of details certainly would enhance the fidelity of the study. However, it would significantly increase the effort of model reconstruction as well as numerical modeling. In fact, as discussed in Secs. 2 and 3, the flow pattern produced by the current simplified model is found in a good agreement with the in-vivo measurement. It indicates that the simulated flow is a reasonable representation of the real cardiac flow. Furthermore, the simplified model produced a well-defined parametric space which is easier to extract the underling mechanism compared with the patient-specific model. The simulations, however, should be interpreted carefully for a specific pathological condition.

Acknowledgment

This research was also supported in part by the National Science Foundation through TeraGrid resources provided by NICS under Grant No. TG-CTS100002.

Reference

[1] Wang, Z., Jalali, F., Sun Y., Wang, J., Parker, K., and Tyberg, J., 2005, "Assessment of LV Diastolic Suction in Dogs Using Wave-Intensity Analysis," Am. J. Physiol. Heart Circ. Physiol., **288**, pp. H1641–H1651.
[2] Courtois, M., Kovacs, S. J., and Ludbrook, P., 1988, "Transmitral Pressure-Flow Velocity Relation. Importance of Regional Pressure Gradients in the Left Ventricle During Diastole," Circulation, **78**, pp. 661–671.
[3] Bronzino, J. D., 1999, *The Biomedical Engineering Handbook*, 2nd ed., CRC Press, Boca, Raton, FL.
[4] Smiseth, O. A., and Tendera, M., 2008, *Diastolic Heart Failure*, Springer, London.
[5] Carcia, J. M., Smedira, N. G., Greenberg, N. L., Main, M., Firstenberg, M. S., Odabashian, J., and Thomas, J. D., 2000, "Color M-Mode Doppler Flow Propagation Velocity is a Preload Insensitive Index of LV Relaxation: Animal and Human Validation," J. Am. Coll. Cardiol., **35**, pp. 201–208.
[6] Leite-Moreira, A. F., Correia-Pinto, J., and Gillebert, T. C., 2001, "Diastolic Dysfunction and Hypertension," New Engl. J. Med., **341**, pp. 1401–1402.
[7] Redfield, M., Jacobsen, S., Burnett, J., Mahoney, D., Balley, K., and Rodeheffer, R., 2003, "Burden of Systolic and Diastolic Ventricular Dysfunction in the Community: Appreciating the Scope of the Heart Failure Epidemic," JAMA, **289**(2), pp. 194–202.
[8] Carlhäll, C. J., and Bolger, A., 2010, "Passing Strange: Flow in the Failing Ventricle," Circ.: Heart Failure, **3**, pp. 326–331.
[9] Domenichini, F., Pederizzetti, G., and Baccani, B., 2005, "Three-Dimensional Filling Flow Into a Model Left Ventricle," J. Fluid Mech., **539**, pp. 179–198.
[10] Lemmon, J. D., and Yoganathan, A. P., 2000, "Computational Modeling of Left Heart Diastolic Function: Examination of Ventricular Dysfunction," ASME J. Biomech. Eng., **122**, pp. 297–303.
[11] Shenkel, T., Malve, M., Reik, M., Markl, M., Jung, B., and Oertel, H., 2009, "MRI-Based CFD Analysis and Application to Healthy Heart," Ann. Biomed. Eng., **37**, pp. 503–515.
[12] Kheradvar, A., Assadi, R., Falahatpisheh, A., and Sengupta, P., 2011, "Assessment of Transmitral Vortex Formation in Patients With Diastolic Dysfunction," J. Am. Soc. Echocardiogr., **25**, pp. 220–227.

[13] Ishizu, T., Seo, Y., Ishimitsu, T., Obara, K., Moriyama, N., Kawano, S., Watanabe, S., and Yamaguchi, I., 2006, "The Wake of a Large Vortex is Associated With Intraventricular Filling Delay in Impaired Left Ventricles With a Pseudonormalized Transmitral Flow Pattern," Echocardiography, **23**, pp. 368–375.
[14] Baccani, B., Domenichini, F., and Pedrizzetti, G., 2002, "Vortex Dynamics in a Model Left Ventricle During Filling," Eur. J. Mech., B, **21**, pp. 527–543.
[15] Domenichini, F., Querzoli, G., Genedese, A., and Pedrizzetti, G., 2007, "Combined Experimental and Numerical Analysis of the Flow Structure into the Left Ventricle," J. Biomech., **40**, pp. 1988–1994.
[16] Hong, G., Pedrizzetti, G., Tonti, G., Li, P., Wei, Z., Kim, J., Baweja, A., Liu, S., Chung, N., Houle, H., Narula, J., and Vannan, M., 2008, "Characterization and Quantification of Vortex Flow in the Human Left Ventricle by Contrast Echocardiography Using Vector Particle Image Velocimetry," JACC Cardiovasc. Imaging, **1**, pp. 705–717.
[17] Kheradar, A., Houle, H., Pedrizzetti, G., Tonti, G., Belcik, T., Ashraf, M., Lindner J., Gharib, M., and Sahn, D., 2010, "Echocardiographic Particle Image Velocimetry: A Novel Technique for Quantificatioin of LV Blood Vorticity Pattern," J. Am. Soc. Echocardiogr., **23**, pp. 86–94.
[18] Gharib, M., Rambod, E., and Shariff, K., 1998, "A universal Time-Scale of Vortex Formation Time," ASME J. Fluid Mech., **360**, pp. 121–141.
[19] Gharib, M., Rambod, E., Kheradvar, A., Sahn, D. J., and Dabiri, J. O., 2006, "Optimal Vortex Formation as an Index of Cardiac Health," Proc. Natl. Acad. Sci., **103**(16), pp. 6305–6308.
[20] Kheradvar, A., Assadi, R., Falahatpisheh, A., and Sengupta, P. P., 2012, "Assessment of Transmitral Vortex Formation in Patients with Diastolic Dysfunction," J. Am. Soc. Echocardiogr., **25**(5), pp. 220–227.
[21] Kilner, P., Yang, G., Wilkes, A., Mohiaddin, R., Firmin, D., and Yacoub, M., 2000, "Asymmetric Redirection of Flow Through the Heart," Nature, **404**, pp. 759–761.
[22] Pedrizzetti, G., and Domenichini, F., 2005, "Nature Optimizes the Swirling Flow in the Human Left Ventricle," Phys. Rev. Lett., **95**, p. 108101.
[23] Mangual, J., Krainer, E., De Luca, A., Toncelli, L., Shah, A., Solomon, S., Galanti, G., Domenichini, F., and Pedrizzetti, G., 2013, "Comparative Numerical Study on LV Fluid Dynamics After Dilated Cardiomyopathy," J. Biomech., **46**, pp. 1611–1617.
[24] Shorland, A. P., Black, R. A., Jarvis, J. C., Henry, S., Iudicello, F., and Collins, M. W., 1996, "Formation and Travel of Vortices in Model Ventricles: Application to the Design of Skeletal Muscle Ventricles," J. Biomech., **4**, pp. 503–511.
[25] Kheradvar, A., Milano, M., and Gharib, M., 2007, "Correlation Between Vortex Ring Formation and Mitral Annulus Dynamics During Ventricular Rapid Filling," ASAIO J., **53**, pp. 8–16.
[26] Mandinov, L., Eberli, F. R., Seiler, C., and Hess, O. M., 2000, "Review: Distolic Heart Failure," Cardiovasc. Res., **45**, pp. 813–825.
[27] Pierrakos, O., and Vlachos, P., 2006, "The Effect of Vortex Formation on LV Filling and Mitral Valve Efficiency," ASME J. Biomech. Eng., **128**, pp. 527–539.
[28] Zhong, L., Su, Y., Gobeawan, L., Sola, S., Tan, R., Navia, J., Ghista, D., Chua, T., Guccione, J., and Kassab, G., 2011, Impact of Surgical Ventricular Restoration on Ventricular Shape, Wall Stress, and Function in Heart Failure Patients," Am. J. Physiol. Heart Circ. Physiol., **300**, pp. 1653–1660.
[29] Le, T., and Sotiropoulos, F., 2012, "On the Three-Dimensional Vortical Structure of Early Diastolic Flow in a Patient-Specific Left Ventricle," Eur. J. Mech. B, **35**, pp. 20–24.
[30] Nakanura, M., Wada, S., Mikami, T., Kitabatake, A., and Karino, T., 2003, "Computational Study on the Evolution of an Intraventricular Vortical Flow During Early Diastole for the Interpretation of Color M-Mode Doppler Echocardiograms," Biomech. Model. Mechanobiol., **2**, pp. 59–72.
[31] Georgiadis, M., and Pasipoularides, A., 1992, "Computational Fluid Dynamics of LV Ejection," Ann. Biomed. Eng., **20**, pp. 81–97.
[32] Domenichini, F., and Pedrizzetti, G., 2011, "Intraventricular Vortex Flow Changes in the Infracted Left Ventricle: Numerical Results in a Idealized 3D Shape," Comput. Methods Biomech. Biomed. Eng., **14**(1), pp. 95–101.
[33] Talor, T., Okino, H., and Yamaguchi, T., 1994, "Three Dimensional Analysis of LV Ejection Using Computational Fluid Dynamics," ASME J. Biomech. Eng., **116**, pp. 127–130.
[34] Watanabe, H., Sugiura, S., Kafuku, H., and Hisada, T., 2004, "Multiphysics Simulation of Left Ventricle Filling Dynamics Using Fluid-Structure Interaction Finite Element Method," Biophys. J., **87**, pp. 2074–2085.
[35] Nichols, W., O'Rourke, M., and Vlachopoulos, C., 2011, *McDonald's Blood Flow in Arteries: Theoretical, Experimental and Clinical Principles*, 6th ed., CRC Press, Boca Raton, FL.
[36] Mittal, R., Dong, H., Bozkuittas, M., Najiar, F. M., Vargas, A., and Loebbecke, A., 2008, "A Versatile Sharp Interface Immersed Boundary Method for Incompressible Flows With Complex Boundaries," J. Comput. Phys., **227**(10), pp. 4825–4852.
[37] Arts, W. C., Hunter, A., Douglas, M. M., Muijtjens, and R. S. Reneman, 1992, "Description of the Deformation of the LV by a Kinematic Model," J. Biomech., **25**, pp. 1119–1127.
[38] Yoganathan, A., He, Z., and Jones, S. C., 2004, "Fluid Mechanics of Heart Valves," Annu. Rev. Biomed. Eng., **6**, pp. 331–362.
[39] Eriksson, J., Carlhall, C., Dyverfeldt, P., Engvall, J., Bolger, A., and Ebbers, T., 2010, "Semi-Automatic Quantification of 4d LV Blood Flow," J. Cardiovasc. Magn. Reson., **12**, p. 9.
[40] Markl, M., Kilner, P., Ebbers, T., 2011, "Comprehensive 4d Velocity Mapping of the Heart and Great Vessels by Cardiovascular Magnetic Resonance," J. Cardiovasc. Magn. Reson., **13**, p. 7.
[41] Pasipoularides, A., 2009, *Heart's Vortex: Intracardiac Blood Flow Phenomena*, PMPH-USA, Shelton, CT.
[42] Charonko, J., Kumar, R., Stewart, K., Little, W., and Vlachos, P., 2013, "Vortices Formed on the Mitral Valve Tips Aid Normal LV Filling," Ann. Biomed. Eng., **41**(5) pp. 1049–1061.
[43] Olcay, A. B., and Krueger, P. S., 2008, "Measurement of Ambient Fluid Entrainment During Laminar Vortex Ring Formation," Exp. Fluids, **44**, pp. 235–247.
[44] Töger, J., Kanski, M., Carlsson, M., Kovacs, S. J., Soderlind, G., Arhenden, H., and Heiberg, E., 2012, "Vortex Ring Formation in the Left Ventricle of the Heart: Analysis by 4D Flow MRI and Lagrangian Coherent Structure," Ann. Biomed. Eng., **40**, 2652–2662.
[45] Hendabadi, S., Bermejo, J., Benito, Y., Yotti, R., Fernandez-Aviles, F., Alamo, J. C., and Shadden, S., 2013, "Topology of Blood Transport in the Human Left Ventricle by Novel Processing of Doppler Echocardiography," Ann. Biomed. Eng., **41**, pp. 2603–2616.